

Matching Free Depth Recovery from Structured Light

Zhuohang Yu¹ Kai Wang² Juyong Zhang^{1*}

¹University of Science and Technology of China ²China Unicom

Abstract

We present a novel approach for depth estimation from images captured by structured light systems. Unlike many previous methods that rely on image matching process, our approach uses a density voxel grid to represent scene geometry, which is trained via self-supervised differentiable volume rendering. Our method leverages color fields derived from projected patterns in structured light systems during the rendering process, enabling the isolated optimization of the geometry field. This contributes to faster convergence and high-quality output. Additionally, we incorporate normalized device coordinates (NDC), a distortion loss, and a novel surface-based color loss to enhance geometric fidelity. Experimental results demonstrate that our method outperforms existing matching-based techniques in geometric performance for few-shot scenarios, achieving approximately a 60% reduction in average estimated depth errors on synthetic scenes and about 30% on real-world captured scenes. Furthermore, our approach delivers fast training, with a speed roughly three times faster than previous matching-free methods that employ implicit representations.

1. Introduction

With the advent of structured-light cameras such as Kinect V2 and Intel RealSense [17], structured light systems have become a powerful solution for range sensing in various applications [4, 31, 32, 42]. Typically, a monocular structured light system consists of one camera and one projector, both with calibrated intrinsic and extrinsic parameters. By projecting randomly or manually designed patterns into 3D space, the system extracts depth information by analyzing the deformation of these patterns in captured images. Classical algorithms in structured light aim to establish robust correspondences across multiple projected patterns, as illustrated in Fig. 1.

The 3D scanning process in structured light systems often requires balancing the trade-off between scan precision and the number of projected patterns or captured images.

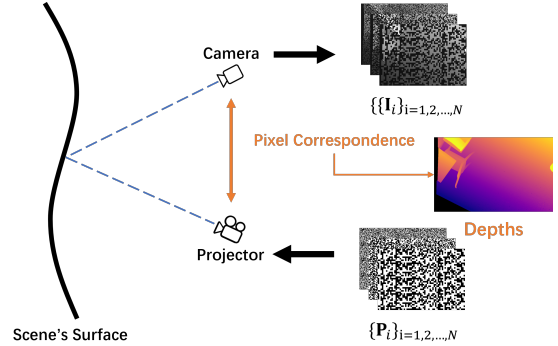


Figure 1. An illustration of a monocular structured light system. Depth is computed by pixel correspondences between camera and projector. These correspondences are typically calculated through image matching algorithms.

Increasing the number of captured images can improve the accuracy of correspondence matching. However, more projected patterns also lead to longer acquisition times, which limits the applicability of structured light systems in general scenes, especially those with undesired motion and short exposure times. To address this, researchers have developed techniques to embed richer information within a limited set of patterns [11, 12, 14, 23, 46]. These methods use sophisticated patterns that encode temporal or spatial features to mitigate matching uncertainties. By decoding these features from captured images, structured light systems can determine the correspondences needed for accurate depth estimation [16, 18, 29, 30].

Despite these advances, designing features that can produce accurate dense depth maps while remaining resilient to environmental influences remains a significant challenge. Traditional structured light depth recovery methods rely on the accuracy of the matching algorithm between projected patterns and captured images. Any errors in the matching process, such as blurring or occlusions, can introduce substantial inaccuracies in the final depth maps. Recent deep learning techniques offer solutions by using neural networks to tackle matching uncertainties [15, 26, 28]. Most of these methods train a general model that is then used to directly predict depth. While these models can generate dense

*Corresponding author

depth maps, they require extensive training datasets, which can significantly impact network performance. Constructing such datasets is challenging in structured light systems, given the diversity of devices and pattern configurations involved.

Our work draws inspiration from recent success in using classic voxel grids to explicitly store scene geometries [9, 13, 47]. Instead of focusing on designing or learning robust matching features, we introduce a novel framework based on volume rendering. Specifically, our approach employs a voxel grid to represent the volume density of the target 3D scene. Through a fully differentiable rendering process, we generate images from the camera’s viewpoint, calculating color from projected patterns, and establish a straight training pipeline with a direct loss function between the captured images and their rendered counterparts. Once training converges, the volume density of the 3D space is obtained, enabling the extraction of both the scene’s geometry and the depth map via simple volumetric rendering. The rendering pipeline in our approach is similar to NeRF-based techniques used in view synthesis tasks [22, 48, 49]. While these methods achieve impressive results in image synthesis from passive views, they face limitations in geometry recovery due to the need to jointly estimate radiance and geometry fields from captured images [24, 38, 44, 45]. In structured light systems, however, the radiance field is predetermined by the projected patterns, allowing us to focus solely on optimizing the geometry field for high-quality depth estimation.

We leverage constraints from the projected light field to optimize the 3D voxel grid in a monocular structured light setup. This process includes a rendering mechanism that incorporates these projected pattern constraints during ray sampling. Additionally, we introduce a distortion loss to accelerate training and a surface color loss to enhance geometric accuracy. Our experimental results demonstrate that, with as few as six randomly generated binary patterns, our method significantly outperforms existing matching-based techniques in terms of geometric accuracy. Specifically, it reduces the average estimated depth error by approximately 60% on synthetic scenes and by around 30% on real-world captured scenes. Furthermore, our approach offers a substantial advantage in training efficiency, achieving a training speed nearly three times faster than methods that rely on implicit geometry representations.

In summary, the main contributions of our work are as follows:

- We propose a novel matching free framework for depth estimation in structured light systems that eliminates the need for extensive training datasets or specifically designed patterns, which are typically required in traditional matching-based techniques.
- Our method incorporates color information from the

projected patterns as existing color field to train the voxel grid, which facilitates faster convergence and improves geometry estimation performance.

- By using voxel grids for geometry representation in our training process, we achieve efficient volume rendering, which accelerates the overall training optimization process.

2. Related Work

Temporal-encoding structured light systems. Temporal-encoding patterns are widely used in structured light systems for static scene reconstruction, as they enable unique decoding at each camera pixel. The plane of light is in a unique location at each time instant, and can be used to recover depth. A number of strategies for coding space with a time sequence of light patterns have been proposed, including binary strips[33], gray codes [1, 25, 40], grid patterns [19], fringe patterns [16, 18, 30, 37], and phase measurements [39, 51]. Modern structured light systems achieve high accuracy and resilience to noise when sufficient patterns are projected. However, this accuracy declines significantly in few-shot scenarios where only a limited number of patterns can be projected. To address this limitation, researchers have explored enhanced coding strategies, such as using specialized devices [1, 36, 40], complex pattern designs [19, 33], or global optimization methods during post-processing [16, 18, 29, 30]. Despite these efforts, manually modeling uncertain factors often introduces unstable outliers in the depth map estimation.

Learning-based matching in structured light systems. Learning-based methods have been increasingly applied to address the matching problem in structured light systems, as demonstrated in studies like [7, 8]. Some other works employ deep networks to directly predict disparity from image-pattern pairs within these systems[15, 28, 50]. However, these approaches require extensive training datasets, and the scarcity of publicly available benchmarks tailored to the unique characteristics of structured light—such as specific pattern designs and parameter configurations—presents a significant challenge. Besides, these learning-based method often encounter domain shift issues when applied to real scene settings.

Voxel grid representation for 3D geometry. Voxel grids model 3D objects by dividing space into a regular array of volumetric units, or voxels, each storing data like color, density, or material properties. This approach is advantageous for capturing complex geometries and internal structures, especially when surface-based methods, such as meshes, fall short. Noteworthy applications of voxel grids in deep learning include VoxNet by Maturana and Scherer [21], a 3D CNN that operates on voxel grids for object recognition. Further advancing this integration, VoxGRAF by Schwarz *et al.* [34] introduces a sparse voxel

grid framework for 3D-aware image synthesis, efficiently rendering views with 3D consistency and visual fidelity by combining sparse grids with 3D convolutions, progressive growing, and free-space pruning. DVGO by Cheng Sun *et al.* [35] apply voxel grids to model 3D geometry in neural rendering pipeline [22], which achieves NeRF-comparable quality and converges rapidly from scratch. In this work, we also adopt voxel grid structure to develop a tailored training framework for high-quality depth reconstruction within structured light systems.

3. Methods

Our approach focuses on monocular structured light systems, consisting of a single camera and a projector to capture images for depth estimation. Given a set of patterns $\{\mathbf{P}_i\}_{i=1,2,\dots,N}$, the projector sequentially projects them onto the scene, while the camera captures images $\{\mathbf{I}_i\}_{i=1,2,\dots,N}$. Here, N represents the number of projected patterns. With the known intrinsic and extrinsic parameters of both the camera and the projector, our goal is to reconstruct the depth map \mathbf{D} from the camera viewpoint. As it is under monocular setting, we can simply set the extrinsic matrix of the camera to identity matrix, *i.e.* $c2w = \mathbf{I}_{4 \times 4}$.

Traditional matching-based methods attempt to define a function which use estimated point-by-point correspondences to directly compute the depth map. In contrast, we introduce a novel matching free framework, as shown in Fig. 2. We first build a density voxel grid to store geometric information of the input scene (Sec. 3.1). This is followed by a differentiable volume rendering process to generate camera-observed images (Sec. 3.2). Finally, the network is trained using several loss functions to compare the rendered images with the captured ones (Sec. 3.3).

3.1. Density Voxel Grid

A voxel-grid representation explicitly encodes relevant scene modalities (*e.g.* density, color, or feature) within each grid cell. This structured approach allows for efficient interpolation-based queries at any 3D position, facilitating rapid access to detailed spatial information:

$$\text{interp}(\mathbf{x}, \mathbf{V}) : (\mathbb{R}^3, \mathbb{R}^{C \times N_x \times N_y \times N_z}), \rightarrow \mathbb{R}^C, \quad (1)$$

where x denotes the queried 3D point, V represents the voxel grid, C is the modality dimension, and N_x, N_y, N_z is total number of voxels on each dimension. We use trilinear interpolation in our method.

Density voxel grid $\mathbf{V}^{(\text{density})}$ is a special case with $C = 1$, which stores the density values for volume rendering (see Eq.(4)). Similar to DVGO [35], we use $\check{\sigma} \in \mathbb{R}$ to denote the raw density stored by the voxel grid. We then use the shifted softplus from Mip-NeRF [2] to apply the density activation:

$$\sigma = \text{softplus}(\check{\sigma}) = \log(1 + \exp(\check{\sigma} + b)). \quad (2)$$

All grid values in $\mathbf{V}^{(\text{density})}$ are initially set to zero. To ensure that all sampled points on rays are visible to the camera at the start, we initialize the accumulated transmittance $T_i \approx 1$ by setting the shift b to

$$b = \log \left(\left(1 - \alpha^{(\text{init})} \right)^{-\frac{1}{\delta}} - 1 \right), \quad (3)$$

where $\alpha^{(\text{init})}$ serves as a hyperparameter, and δ is the step size. Employing the softplus function instead of ReLU is essential for optimizing voxel density, as ReLU may irreversibly set it to zero when a voxel value is falsely set to negative.

3.2. Rendering with Projected Patterns

For one of the captured image \mathbf{I}_j , we define its corresponding rendered image as $\hat{\mathbf{I}}_j$. To render the color of a pixel $\hat{\mathbf{I}}_j(\mathbf{r})$, we cast the ray \mathbf{r} from the camera center through the pixel. K points are then sampled on \mathbf{r} between the predefined near and far planes. The K ordered sampled points are then used to query for their densities and colors $\{(\sigma_i, \mathbf{c}_i)\}_{i=1}^K$. Finally, the K queried results are accumulated into a single color with the volume rendering equation [22]:

$$\begin{aligned} \hat{\mathbf{I}}_j(\mathbf{r}) &= \left(\sum_{i=1}^K T_i \alpha_i \mathbf{c}_i \right) \\ \alpha_i &= 1 - \exp(-\sigma_i \delta_i) \\ T_i &= \prod_{j=1}^{i-1} (1 - \alpha_j), \end{aligned} \quad (4)$$

where α_i is the probability of termination at point \mathbf{x}_i ; T_i is the accumulated transmittance from the near plane to point i , and δ_i is the distance to the adjacent sampled point.

We use post-activation strategy from [35] to calculate the density of the sampled point \mathbf{x}_i . That means we first use trilinear interpolation to get the raw density value:

$$\check{\sigma}_i = \text{interp} \left(\mathbf{x}_i, \mathbf{V}^{(\text{density})} \right) \quad (5)$$

We then employ the softplus function (Eq.(2)) to get σ_i , and finally use it to calculate rendered results. DVGO [35] has shown that post-activation strategy can produce a sharp linear boundary.

In our approach, the color of the sampled point \mathbf{x}_i is not estimated from voxel grid or network architecture. Instead, we utilize prior knowledge from our projected patterns to determine the point color using a re-projection function π . Specifically, the color \mathbf{c}_i can be directly calculated from the projected pattern \mathbf{P}_j through:

$$\mathbf{c}_i = B(\mathbf{r}) + F(\mathbf{r})\mathbf{P}_j(\pi(\mathbf{x}_i)), \quad (6)$$

where \mathbf{r} is the sampled ray, $\mathbf{P}_j(\pi(\mathbf{x}_i))$ symbolizes the projected color calculated through re-projection operation

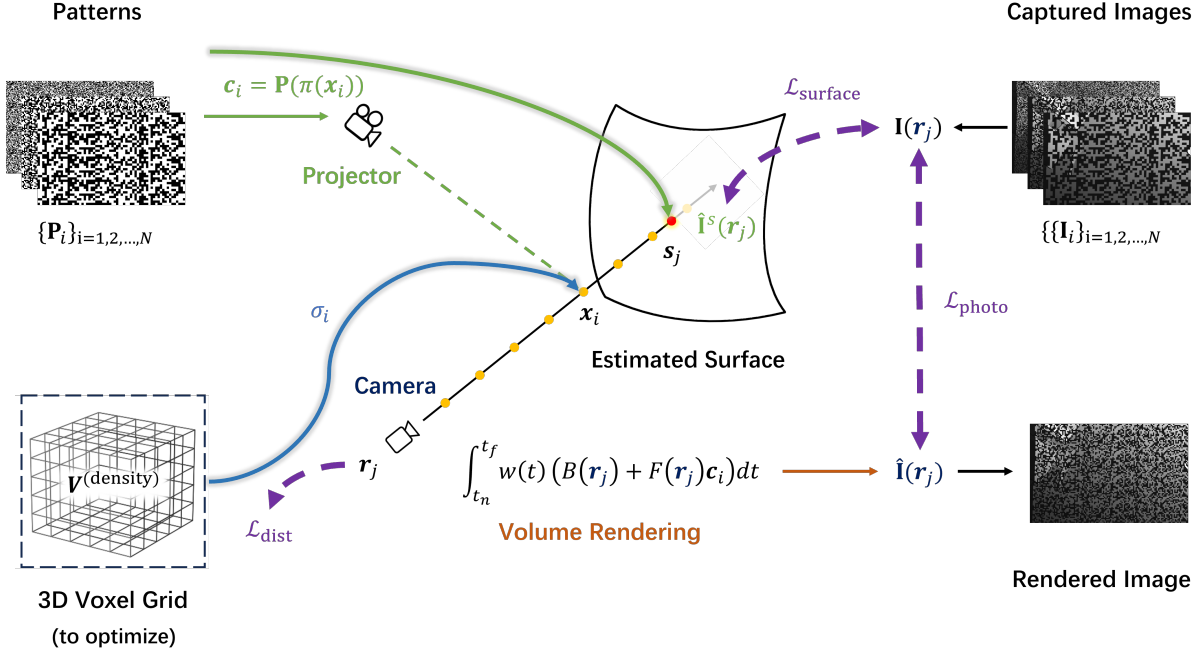


Figure 2. Our pipeline for matching free depth recovery in structured light systems. Sampled rays are rendered through volume rendering process using voxel grid density. Each sampled point on the ray is converted into projector space to query the color. The ray’s rendered color and the color of its estimated surface point are both compared with the captured image to train our voxel grid.

based on the intersection between projected light and sampled ray (note that $\mathbf{P}(\cdot)$ query pixel color on the pattern via its pixel coordinates). $B(\mathbf{r})$ and $F(\mathbf{r})$ stand for the background light level and fringe contrast, respectively. They are calculated from the captured images:

$$\begin{aligned} B(\mathbf{r}) &= \min \left(\{\mathbf{I}_j(\mathbf{r})\}_{j=1,2,\dots,N} \right) \\ F(\mathbf{r}) &= \max \left(\{\mathbf{I}_j(\mathbf{r})\}_{j=1,2,\dots,N} \right) - B(\mathbf{r}). \end{aligned} \quad (7)$$

It is important to highlight that these two parameters inherently enable the masking of occluded regions, as both the fringe contrast and the background light level tend to approach zero in these areas.

3.3. Loss Functions

During the training process, we pick a batch of M pixels from each captured image, and sample K points on each corresponding ray. We then calculate the color of these rays to generate the rendered color $\hat{\mathbf{I}}_j(\mathbf{r})$ for each image j . We first minimize a per-pixel loss function that quantifies the difference between $\hat{\mathbf{I}}(\mathbf{r})$ and the color $\mathbf{I}(\mathbf{r})$ from captured image. The photometric MSE is defined as

$$\mathcal{L}_{\text{photo}} = \frac{1}{MN} \sum_{j=1}^N \sum_{i=1}^M \|\hat{\mathbf{I}}_j(\mathbf{r}_i) - \mathbf{I}_j(\mathbf{r}_i)\|_2^2. \quad (8)$$

In our scenario, the volumetric density along each sampled light ray should be singular peaked, as each ray from

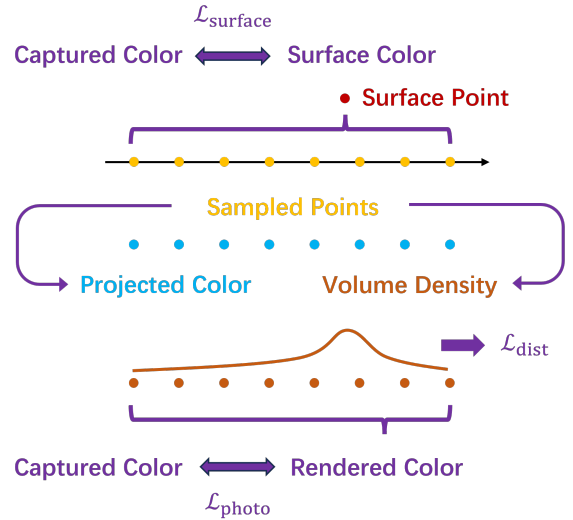


Figure 3. Visualization of our photometric loss $\mathcal{L}_{\text{photo}}$, distortion loss $\mathcal{L}_{\text{dist}}$, and surface color loss $\mathcal{L}_{\text{surface}}$. The photometric loss encourages accurate color in rendered images, while both distortion loss and surface color loss enforces a singular peak along the ray.

camera should intersect only once with the object’s surface. Besides, due to the lack of camera views in our task, there may be multiple peaks along the projecting ray to produce one precise color, resulting in lots of floaters in the recon-

structured geometry. Thus we apply a distortion loss proposed by Mip-NeRF 360 [3]. For a ray with K sampled points, this loss is defined as

$$\mathcal{L}_{\text{dist}}(s, w) = \sum_{i=0}^{K-1} \sum_{j=0}^{K-1} w_i w_j \left| \frac{s_i + s_{i+1}}{2} - \frac{s_j + s_{j+1}}{2} \right| + \frac{1}{3} \sum_{i=0}^{K-1} w_i^2 (s_{i+1} - s_i), \quad (9)$$

where $(s_{i+1} - s_i)$ is the length, $(s_i + s_{i+1})/2$ is the midpoint of the i -th query interval and $w_i = T_i \alpha_i$. The first term minimizes the weighted distances between all pairs of interval midpoints, and the second term minimizes the weighted size of each individual interval. As a result, the trained geometry is forced to fit our task. The total distortion loss is

$$\mathcal{L}_{\text{dist-total}} = \frac{1}{MN} \sum_j \sum_i \mathcal{L}_{\text{dist}}. \quad (10)$$

We additionally introduce another color loss to deal with those artifacts. We first compute the rendered surface point of a ray \mathbf{r}_l using a volume rendering equation similar to Eq.(4) :

$$\mathbf{s}_l = \left(\sum_{i=1}^K T_i \alpha_i \mathbf{x}_i \right). \quad (11)$$

Then Eq.(6) is applied to compute the pixel color of \mathbf{s}_l as

$$\widehat{\mathbf{I}}_j^s(\mathbf{r}_l) = B(\mathbf{r}_l) + F(\mathbf{r}_l) \mathbf{P}_j(\pi(\mathbf{s}_l)). \quad (12)$$

We formulate the surface color loss as

$$\mathcal{L}_{\text{surface}} = \frac{1}{MN} \sum_{j=1}^N \sum_{i=1}^M \|\widehat{\mathbf{I}}_j^s(\mathbf{r}_i) - \mathbf{I}_j(\mathbf{r}_i)\|_2^2. \quad (13)$$

The surface color loss is similar to photometric constraints which are applied in matching-based techniques [10, 50], where colors are warped between images using pixel depth information. It can enhance geometry quality and overall performance, especially in few-shot scenarios [6, 24, 43]. Our approach prioritizes geometric performance over photorealism. Therefore, enforcing density constraints helps the network generate more accurate 3D shapes without introducing rendering ambiguities. We provide a schema to illustrate the difference between rendered color loss and surface color loss in Fig. 3.

The whole loss function is defined as

$$\mathcal{L} = \mathcal{L}_{\text{photo}} + \lambda_d \mathcal{L}_{\text{dist-total}} + \lambda_s \mathcal{L}_{\text{surface}}. \quad (14)$$

Once the training process is finished, we extract the full depth map \mathbf{D} of input scene using Eq.(11).

3.4. NDC Parameterization

Our task focuses on front-facing scenes, as there’s only one camera in a monocular structured light system. Inspired by the original NeRF [22], we define our voxel grid in normalized device coordinates(NDC) space. By warping an infinitely deep camera frustum into a bounded cube, where distance along the z-axis corresponds to disparity (inverse distance), NDC efficiently reallocates the voxel grid’s density in a way that aligns with the geometry of perspective projection.

It is important to note that NDC is particularly well-suited for our task. When we uniformly sample points along a ray in NDC space, these samples are uniformly spaced in disparity. According to our projection matrix \mathbf{P} , the offset between two sampled points along a camera ray in pattern coordinates is also proportional to disparity. As a result, the sampled points are evenly distributed across the patterns.

4. Experiments

4.1. Datasets

We use patterns as color constraints for training the voxel grid to represent 3D scene geometry, eliminating the need for explicit matching techniques typically applied to pattern sets. Thus, we simply use a set of randomly generated, array-based patterns. The projector space is divided into uniform squares, with each square randomly assigned either black or white. To generate our pattern sets, we use unit squares of varying sizes. We select pattern lengths of 20, 10, and 5 pixels to generate a total of 6 patterns (two patterns per scale) for experiments, same as in SL-SDF [27].

To evaluate our approach and compare it with existing methods, we first assess the accuracy of depth estimation on synthetic scenes. These scenes are rendered using the tool provided by CTD [28], following the same experimental setup as CTD and using objects from the ShapeNet dataset [5]. A total of 50 different scenes were rendered to create our synthetic dataset. The camera’s intrinsic parameters and the projector’s settings are similar to those used in SL-SDF [27] to facilitate later comparison. Additionally, we test our method on a real dataset provided by [27], which includes 6 scenes with estimated ground truth depths.

4.2. Implementation Details

We use consistent hyperparameters across all scenes. We divide the xy-plane of the NDC cube to 256×256 and discretize the length along the z-axis into 256 different disparity values, resulting in an expected voxel count of $M = 256^3$. We set $\alpha^{(\text{init})} = 10^{-2}$ and the point sampling step size is chosen as half of the voxel size. For training the voxel grid, we use $\lambda_d = 0.01$ with $\lambda_s = 0$ for the first 3000 iterations, during which we sample 8192 rays per iteration. The exclusion of surface color loss during this phase is a

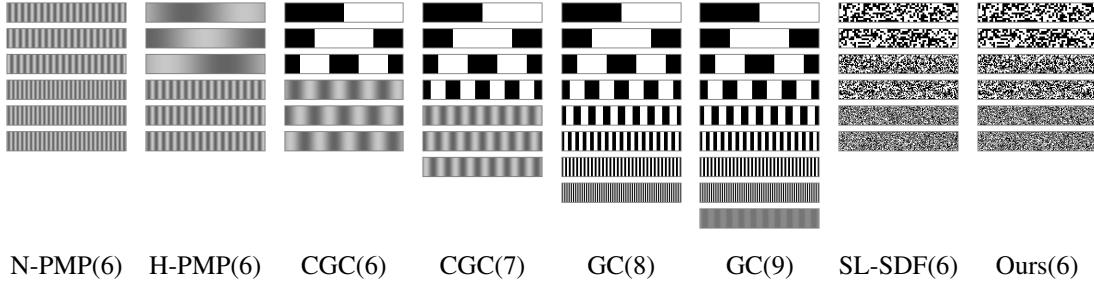


Figure 4. Pattern sets used by different methods. Note that they are vertically repetitive.

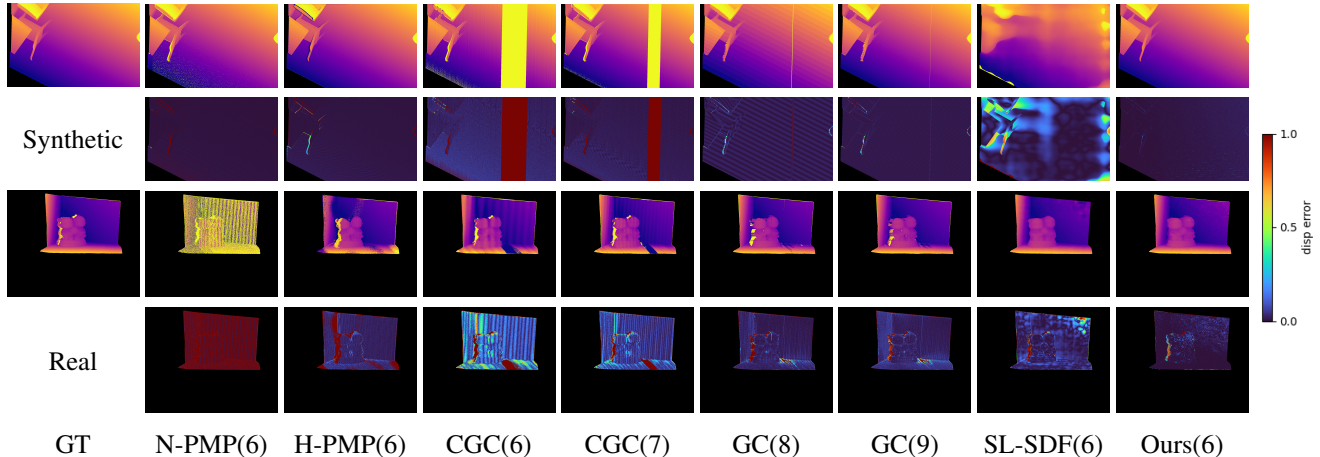


Figure 5. Visualization of estimated depths and error maps by different methods on both synthetic and real scene. The disparity differences between estimated results and ground truth are displayed in the second and fourth rows.

strategic choice to avoid potential issues with local minima. After the initial phase, we set $\lambda_s = 1$ and continue training for an additional 29,000 iterations. The entire training process takes approximately 5 minutes on a single NVIDIA GTX 4060.

4.3. Comparisons

We first evaluate our method against four classic decoding-based structured light techniques, as the core principles of temporal-encoding structured light methods have remained unchanged over the past decade. Specifically, we compare with Numerical Phase Measurement Profilometry (N-PMP) [51], Hierarchical Phase Measurement Profilometry (H-PMP) [39], Binary Gray Code (GC) with interpolation between fringes [1, 25, 40], and Complementary Gray Code (CGC) [41]. N-PMP and H-PMP both require six patterns for decoding, and CGC require six or seven patterns. GC method can take different number of patterns for calculation, here we choose eight and nine for comparison. We also compare our method with SL-SDF [27], which is also a matching free approach. [27] builds a neural signed distance field to represent 3D geometry, and applies a NeuS-based [38] differentiable rendering scheme during training

phase. The depth map is then generated through marching cubes algorithm [20] and re-projection from the trained SDF. The specific patterns used by each method are illustrated in Fig.4, with the corresponding pattern counts indicated in parentheses. To make competitive experiments against SL-SDF, our 2D pattern sets are set to the same as theirs. We use both the average L1 loss and the outlier metric to evaluate the recovered depth maps of each method. The definition of percentage of outliers $o(t)$ is from CTD [28], which is the percentage of pixels where the difference between the estimated and ground-truth disparities (inverse depths) is greater than a certain threshold t . We summarize our experimental results and show them in Table 1. Results shown in the table represent the average depth error and percentage of outliers on each scene in the dataset. Additionally, we visualize estimated images in Fig. 5. The first row shows visualizations of the disparity maps generated by various methods on our synthetic scenes, while the second row presents the error maps between the estimated disparities and the ground truth. The subsequent two rows display the corresponding results on real data. Here disparities are used for better visualization.

The N-PMP, H-PMP, and CGC methods utilize phase-

Method	synthetic scenes					real scenes				
	err:avg	$O(0.1)$	$O(0.5)$	$O(1)$	$O(2)$	err:avg	$O(0.1)$	$O(0.5)$	$O(1)$	$O(2)$
N-PMP(6) [51]	87.461	1.80	1.62	1.32	0.65	513.855	68.99	67.13	62.22	43.01
H-PMP(6) [39]	40.192	0.49	0.15	0.15	0.14	56.635	14.52	3.11	2.12	0.40
CGC(6) [41]	83.594	1.32	0.90	0.84	0.75	46.857	7.05	5.29	0.81	0.50
CGC(7) [41]	69.538	1.02	0.89	0.49	0.38	38.849	6.00	3.90	1.52	0.53
GC(8) [1, 40]	56.567	0.65	0.61	0.56	0.45	18.941	4.92	3.17	2.20	0.63
GC(9) [1, 40]	43.715	0.55	0.50	0.41	0.23	16.171	4.30	2.19	1.23	0.56
SL-SDF(6) [27]	42.056	0.49	0.39	0.39	0.39	9.376	3.14	0.82	0.45	0.31
Ours	13.767	0.08	0.06	0.06	0.06	9.153	2.87	0.92	0.47	0.40

Table 1. The experiment results compared with classic methods on both synthetic and real scenes. The unit of length for "err:avg" here is millimeter. Results on the synthetic dataset represent the average values across 50 scenes, and those on the real dataset are an average of 6 scenes. We color code the **best** and **second best**.

Losses	synthetic scenes					real scenes				
	err:avg	$O(0.1)$	$\$O(0.5)$	$\$O(1)$	$\$O(2)$	err:avg	$O(0.1)$	$\$O(0.5)$	$\$O(1)$	$\$O(2)$
$\mathcal{L}_{\text{photo}}$	35.844	0.21	0.12	0.11	0.11	38.712	7.13	4.69	1.91	0.54
$\mathcal{L}_{\text{photo}} + \mathcal{L}_{\text{dist-total}}$	27.210	0.15	0.12	0.11	0.11	33.948	6.74	3.81	1.49	0.52
$\mathcal{L}_{\text{photo}} + \mathcal{L}_{\text{surface}}$	18.573	0.10	0.07	0.06	0.06	14.394	3.38	1.51	0.98	0.65
$\mathcal{L}_{\text{photo}} + \mathcal{L}_{\text{dist-total}} + \mathcal{L}_{\text{surface}}$	13.767	0.08	0.06	0.06	0.06	9.153	2.87	0.92	0.47	0.40

Table 2. Ablation studies conducted to assess the impact of the rendered color loss, the distortion loss and the surface color loss. Numbers here also represent the average results of all scenes. We color code the **best** and **second best**.

shifting encoding, which encodes the coordinates into a set of sinusoidal patterns. However, these patterns are periodic, introducing phase ambiguities during decoding. Typically, this issue is addressed by projecting additional patterns with different frequencies. While phase-shifting techniques can achieve high precision with a large number of patterns, they encounter challenges when the pattern count is limited. N-PMP uses two sets of phase patterns with shorter wavelengths, making it sensitive to errors in the decoded phase values. In contrast, H-PMP adds an extra set of phase patterns with a wavelength equivalent to the image width, but it remains susceptible to shading effects. CGC utilizes binary gray-code patterns, but the long wavelengths of these patterns reduce its decoding accuracy. GC relies entirely on binary gray-code patterns, which can lead to inaccuracies between the projected binary fringes

In contrast to traditional methods, both SL-SDF [27] and our approach utilize 2D binary patterns without the need for pattern matching. Experiments demonstrate that both methods are capable of generating smooth surfaces. However, SL-SDF struggles on certain synthetic datasets, particularly those containing sharp surface edges or complex geometries. This limitation stems from its use of signed distance fields (SDFs). While SDFs effectively enforce surface smoothness, they face difficulties in modeling sharp geometric features, as shown in Fig. 6. This issue be-

comes more pronounced in structured light depth reconstruction scenarios, where textures and color information are reduced. As a result, fine details and sharp edges may be smoothed out or inaccurately reconstructed, impacting the overall fidelity of the recovered depth. In contrast, our voxel-grid-based representation offers significant advantages in handling such scenarios. Unlike SDFs, voxel grids explicitly model scene properties at discrete volumetric locations, enabling more accurate encoding of abrupt geometric changes and providing greater flexibility in capturing sharp edges. The surface color loss and distortion loss we apply ensure the smoothness of our estimated depths while maintaining geometric accuracy.

4.4. Ablation Studies

To evaluate the impact of the loss terms introduced in Section 3.3, we conduct experiments with different combinations of loss functions on our synthetic datasets. The results, presented in Table 2, demonstrate that the primary photometric loss, while effective in reconstructing the overall scene geometry, struggles to capture fine-grained details accurately. The addition of surface color loss significantly improves the representation of these finer geometric features. Furthermore, the distortion loss, which enforces a singular peak along each sampled ray, further enhances the final depth estimation performance.

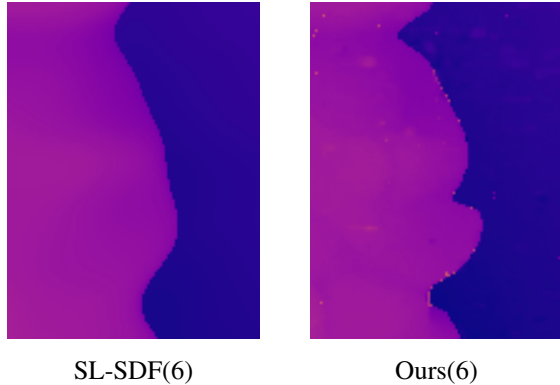


Figure 6. Difference of the estimated depth map at object edges between our method and SL-SDF [27]. SDFs tend to generate smooth surfaces, making it challenging to handle sharp edges.

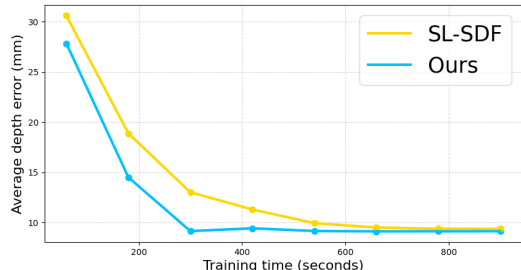


Figure 7. Comparison with SL-SDF on training time and accuracy. We use the same set of 6 patterns as in their approach. Our training converges after 5 minutes while theirs need over 14 minutes.

In order to demonstrate the advantages of our voxel grid training schedule for structured-light-based depth recovery, we make further comparison with SL-SDF [27], which uses signed distance fields (SDFs) for a similar procedure. We explore the relationship between training time and depth estimation accuracy for both methods. As shown in Fig. 7, our method requires significantly less training time to achieve the same level of depth reconstruction accuracy. This efficiency can be attributed to several factors, with one of the main reasons being the inherent differences in iteration speed between explicit and implicit scene representations. Specifically, with the same ray sampling batch size, each iteration in our method is approximately 20 times faster than in SL-SDF.

Furthermore, we examine the effect of the number of projected patterns on the performance of our method. We first increase the pattern count to 9 (with 3 patterns per scale) to demonstrate the full result, and then remove one of them after each test. The results demonstrate that our voxel-based training process achieves satisfactory performance with as few as six patterns, with no significant improvement observed by further increasing the number of patterns. In ad-

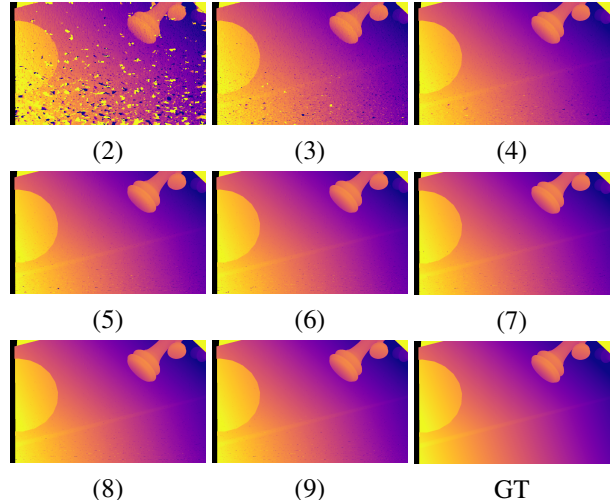


Figure 8. Visualized results of varying pattern numbers. The number below each picture stands for the amount of patterns we used to capture scenes and train our voxel grid. The last one shows the ground truth depth map.

Pat	2	3	4	5	6	7	8
Err	203.9	31.7	18.3	16.9	15.3	15.2	15.0

Table 3. Ablation study on different pattern numbers within our framework. Errors stand for the average depth error across all test scenes. We verify 10 synthetic scenes for this experiment.

dition, our method produces promising results when using only four patterns.

5. Conclusion

In this paper, we proposed a novel framework for depth reconstruction in structured light systems using 3D voxel grids. Our approach centered on training a density voxel grid to represent the geometry of the captured scene, leveraging constraints from projected patterns to guide the training schedule through a fully differentiable rendering process. Upon convergence, we used volume density queried from the trained voxel grid to obtain a depth map through similar rendering approach. The key advantage of our method is that it eliminates the need for traditional correspondence searching on images, thereby removing the reliance on the accuracy of image matching algorithms. Experimental results show that our method yields competitive results compared to traditional matching-based algorithms, while using same or less amount of patterns as theirs. When compared with similar rendering-based method, which use implicit function to represent geometries, our approach demonstrates superior depth estimation accuracy while having faster training speed.

Acknowledgement This research was supported by the National Natural Science Foundation of China (No.62441224, No.62272433), the Fundamental Research Funds for the Central Universities (No.WK001000090). The numerical calculations in this paper have been done on the supercomputing system in the Supercomputing Center of University of Science and Technology of China.

References

- [1] Daniel G Aliaga and Yi Xu. Photogeometric structured light: A self-calibrating and multi-viewpoint framework for accurate 3d modeling. In *CVPR*, pages 1–8. IEEE, 2008. 2, 6, 7
- [2] Jonathan T Barron, Ben Mildenhall, Matthew Tancik, Peter Hedman, Ricardo Martin-Brualla, and Pratul P Srinivasan. Mip-nerf: A multiscale representation for anti-aliasing neural radiance fields. In *ICCV*, pages 5855–5864, 2021. 3
- [3] Jonathan T Barron, Ben Mildenhall, Dor Verbin, Pratul P Srinivasan, and Peter Hedman. Mip-nerf 360: Unbounded anti-aliased neural radiance fields. In *CVPR*, pages 5470–5479, 2022. 5
- [4] Joan Battle, E Mouaddib, and Joaquim Salvi. Recent progress in coded structured light as a technique to solve the correspondence problem: a survey. *PR*, 31(7):963–982, 1998. 1
- [5] Angel X Chang, Thomas Funkhouser, Leonidas Guibas, Pat Hanrahan, Qixing Huang, Zimo Li, Silvio Savarese, Manolis Savva, Shuran Song, Hao Su, et al. Shapenet: An information-rich 3d model repository. *arxiv CS.CV 1512.03012*, 2015. 5
- [6] François Darmon, Bénédicte Bascle, Jean-Clément Devaux, Pascal Monasse, and Mathieu Aubry. Improving neural implicit surfaces geometry with patch warping. In *CVPR*, pages 6260–6269, 2022. 5
- [7] Sean Ryan Fanello, Christoph Rhemann, Vladimir Tankovich, Adarsh Kowdle, Sergio Orts Escolano, David Kim, and Shahram Izadi. Hyperdepth: Learning depth from structured light without matching. In *Proceedings of the IEEE conference on computer vision and pattern recognition*, pages 5441–5450, 2016. 2
- [8] Sean Ryan Fanello, Julien Valentin, Christoph Rhemann, Adarsh Kowdle, Vladimir Tankovich, Philip Davidson, and Shahram Izadi. Ultrastereo: Efficient learning-based matching for active stereo systems. In *CVPR*, pages 6535–6544. IEEE, 2017. 2
- [9] Stephan J Garbin, Marek Kowalski, Matthew Johnson, Jamie Shotton, and Julien Valentin. Fastnerf: High-fidelity neural rendering at 200fps. In *ICCV*, pages 14346–14355, 2021. 2
- [10] Ravi Garg, Vijay Kumar Bg, Gustavo Carneiro, and Ian Reid. Unsupervised cnn for single view depth estimation: Geometry to the rescue. In *ECCV*, pages 740–756. Springer, 2016. 5
- [11] Mohit Gupta and Nikhil Nakhate. A geometric perspective on structured light coding. In *ECCV*, pages 87–102, 2018. 1
- [12] Olaf Hall-Holt and Szymon Rusinkiewicz. Stripe boundary codes for real-time structured-light range scanning of moving objects. In *Proceedings Eighth IEEE International Conference on Computer Vision. ICCV 2001*, pages 359–366. IEEE, 2001. 1
- [13] Peter Hedman, Pratul P Srinivasan, Ben Mildenhall, Jonathan T Barron, and Paul Debevec. Baking neural radiance fields for real-time view synthesis. In *ICCV*, pages 5875–5884, 2021. 2
- [14] Idaku Ishii, Kenkichi Yamamoto, Kensuke Doi, and Tokuo Tsuji. High-speed 3d image acquisition using coded structured light projection. In *IROS*, pages 925–930. IEEE, 2007. 1
- [15] Mohammad Mahdi Johari, Camilla Carta, and François Fleuret. Depthinspace: Exploitation and fusion of multiple video frames for structured-light depth estimation. In *ICCV*, pages 6039–6048, 2021. 1, 2
- [16] Hiroshi Kawasaki, Ryo Furukawa, Ryusuke Sagawa, and Yasushi Yagi. Dynamic scene shape reconstruction using a single structured light pattern. In *CVPR*, pages 1–8. Ieee, 2008. 1, 2
- [17] Leonid Keselman, John Iselin Woodfill, Anders Grunnet-Jepsen, and Achintya Bhowmik. Intel realsense stereoscopic depth cameras. In *CVPRW*, pages 1–10, 2017. 1
- [18] Thomas P Koninckx and Luc Van Gool. Real-time range acquisition by adaptive structured light. *IEEE TPAMI*, 28(3):432–445, 2006. 1, 2
- [19] Yang Lei, Kurt R Bengtson, Lisa Li, and Jan P Allebach. Design and decoding of an m-array pattern for low-cost structured light 3d reconstruction systems. In *ICIP*, pages 2168–2172. IEEE, 2013. 2
- [20] William E Lorensen and Harvey E Cline. Marching cubes: A high resolution 3d surface construction algorithm. In *Seminal graphics: pioneering efforts that shaped the field*, pages 347–353. 1998. 6
- [21] Daniel Maturana and Sebastian Scherer. Voxnet: A 3d convolutional neural network for real-time object recognition. In *IROS*, pages 922–928. IEEE, 2015. 2
- [22] Ben Mildenhall, Pratul P Srinivasan, Matthew Tancik, Jonathan T Barron, Ravi Ramamoorthi, and Ren Ng. Nerf: Representing scenes as neural radiance fields for view synthesis. *ECCV*, pages 405–421, 2020. 2, 3, 5
- [23] Parsa Mirdehghan, Wenzheng Chen, and Kiriakos N Kutulakos. Optimal structured light a la carte. In *CVPR*, pages 6248–6257, 2018. 1
- [24] Michael Niemeyer, Jonathan T Barron, Ben Mildenhall, Mehdi SM Sajjadi, Andreas Geiger, and Noha Radwan. Regnerf: Regularizing neural radiance fields for view synthesis from sparse inputs. In *CVPR*, pages 5480–5490, 2022. 2, 5
- [25] Jeffrey L Posdamer and Martin D Altschuler. Surface measurement by space-encoded projected beam systems. *Computer graphics and image processing*, 18(1):1–17, 1982. 2, 6
- [26] Rukun Qiao, Hiroshi Kawasaki, and Hongbin Zha. Tide: Temporally incremental disparity estimation via pattern flow in structured light system. *RA-L*, 7(2):5111–5118, 2022. 1
- [27] Rukun Qiao, Hiroshi Kawasaki, and Hongbin Zha. Depth reconstruction with neural signed distance fields in structured light systems. In *3DV*, pages 770–779. IEEE, 2024. 5, 6, 7, 8

- [28] Gernot Riegler, Yiyi Liao, Simon Donne, Vladlen Koltun, and Andreas Geiger. Connecting the dots: Learning representations for active monocular depth estimation. In *CVPR*, pages 7624–7633, 2019. 1, 2, 5, 6
- [29] Ryusuke Sagawa, Yuichi Ota, Yasushi Yagi, Ryo Furukawa, Naoki Asada, and Hiroshi Kawasaki. Dense 3d reconstruction method using a single pattern for fast moving object. In *ICCV*, pages 1779–1786. IEEE, 2009. 1, 2
- [30] Ryusuke Sagawa, Hiroshi Kawasaki, Shota Kiyota, and Ryo Furukawa. Dense one-shot 3d reconstruction by detecting continuous regions with parallel line projection. In *ICCV*, pages 1911–1918. IEEE, 2011. 1, 2
- [31] Joaquim Salvi, Jordi Pages, and Joan Batlle. Pattern codification strategies in structured light systems. *PR*, 37(4): 827–849, 2004. 1
- [32] Joaquim Salvi, Sergio Fernandez, Tomislav Pribanic, and Xavier Llado. A state of the art in structured light patterns for surface profilometry. *PR*, 43(8):2666–2680, 2010. 1
- [33] Daniel Scharstein and Richard Szeliski. High-accuracy stereo depth maps using structured light. In *CVPR*, pages I–I. IEEE, 2003. 2
- [34] Katja Schwarz, Axel Sauer, Michael Niemeyer, Yiyi Liao, and Andreas Geiger. Voxgraf: Fast 3d-aware image synthesis with sparse voxel grids. *NeurIPS*, 35:33999–34011, 2022. 2
- [35] Cheng Sun, Min Sun, and Hwann-Tzong Chen. Direct voxel grid optimization: Super-fast convergence for radiance fields reconstruction. In *CVPR*, pages 5459–5469, 2022. 3
- [36] Varun Sundar, Sizhuo Ma, Aswin C Sankaranarayanan, and Mohit Gupta. Single-photon structured light. In *CVPR*, pages 17865–17875, 2022. 2
- [37] Yuichi Taguchi, Amit Agrawal, and Oncel Tuzel. Motion-aware structured light using spatio-temporal decodable patterns. In *ECCV*, pages 832–845. Springer, 2012. 2
- [38] Peng Wang, Lingjie Liu, Yuan Liu, Christian Theobalt, Taku Komura, and Wenping Wang. Neus: Learning neural implicit surfaces by volume rendering for multi-view reconstruction. *NeurIPS*, 34:27171–27183, 2021. 2, 6
- [39] Yajun Wang, Jacob I Laughner, Igor R Efimov, and Song Zhang. 3d absolute shape measurement of live rabbit hearts with a superfast two-frequency phase-shifting technique. *Optics express*, 21(5):5822–5832, 2013. 2, 6, 7
- [40] Michael Weinmann, Christopher Schwartz, Roland Ruiters, and Reinhard Klein. A multi-camera, multi-projector super-resolution framework for structured light. In *International Conference on 3D Imaging, Modeling, Processing, Visualization and Transmission*, pages 397–404. IEEE, 2011. 2, 6, 7
- [41] Zhoujie Wu, Wenbo Guo, Yueyang Li, Yihang Liu, and Qican Zhang. High-speed and high-efficiency three-dimensional shape measurement based on gray-coded light. *Photonics Research*, 8(6):819–829, 2020. 6, 7
- [42] Zhoujie Wu, Wenbo Guo, and Qican Zhang. Two-frequency phase-shifting method vs. gray-coded-based method in dynamic fringe projection profilometry: A comparative review. *Optics and Lasers in Engineering*, 153:106995, 2022. 1
- [43] Yuanbo Xiangli, Linning Xu, Xingang Pan, Nanxuan Zhao, Anyi Rao, Christian Theobalt, Bo Dai, and Dahua Lin. Bungeenerf: Progressive neural radiance field for extreme multi-scale scene rendering. In *ECCV*, pages 106–122. Springer, 2022. 5
- [44] Zike Yan, Yuxin Tian, Xuesong Shi, Ping Guo, Peng Wang, and Hongbin Zha. Continual neural mapping: Learning an implicit scene representation from sequential observations. In *ICCV*, pages 15782–15792, 2021. 2
- [45] Lior Yariv, Jiatao Gu, Yoni Kasten, and Yaron Lipman. Volume rendering of neural implicit surfaces. *NeurIPS*, 34: 4805–4815, 2021. 2
- [46] Mark Young, Erik Beeson, James Davis, Szymon Rusinkiewicz, and Ravi Ramamoorthi. Coded structured light. In *CVPR*, pages 1–8. IEEE, 2007. 1
- [47] Alex Yu, Ruilong Li, Matthew Tancik, Hao Li, Ren Ng, and Angjoo Kanazawa. Plenotrees for real-time rendering of neural radiance fields. In *ICCV*, pages 5752–5761, 2021. 2
- [48] Alex Yu, Vickie Ye, Matthew Tancik, and Angjoo Kanazawa. pixelnerf: Neural radiance fields from one or few images. In *CVPR*, pages 4578–4587, 2021. 2
- [49] Kai Zhang, Gernot Riegler, Noah Snavely, and Vladlen Koltun. Nerf++: Analyzing and improving neural radiance fields. *arxiv CS.CV 2010.07492*, 2020. 2
- [50] Yinda Zhang, Sameh Khamis, Christoph Rhemann, Julien Valentin, Adarsh Kowdle, Vladimir Tankovich, Michael Schoenberg, Shahram Izadi, Thomas Funkhouser, and Sean Fanello. Activestereonet: End-to-end self-supervised learning for active stereo systems. In *ECCV*, pages 784–801, 2018. 2, 5
- [51] Chao Zuo, Qian Chen, Guohua Gu, Shijie Feng, Fangxi-aoyu Feng, Ruben Li, and Guochen Shen. High-speed three-dimensional shape measurement for dynamic scenes using bi-frequency tripolar pulse-width-modulation fringe projection. *Optics and Lasers in Engineering*, 51(8):953–960, 2013. 2, 6, 7